Understanding thermal transport in asymmetric layer hexagonal boron nitride heterostructure

2017 Nanotechnology 28 035404

(http://iopscience.iop.org/0957-4484/28/3/035404)

IOP Publishing Nanotechnology

Nanotechnology **28** (2017) 035404 (9pp) doi:10.1088/1361-6528/28/3/035404

Understanding thermal transport in asymmetric layer hexagonal boron nitride heterostructure

Jingchao Zhang[1,2,7], Xinyu Wang[3], Yang Hong[4], Qingang Xiong[5], Jin Jiang[1,6] and Yanan Yue[1,6,7]

[1] School of Power and Mechanical Engineering, Wuhan University, Wuhan, Hubei 430072, People's Republic of China
[2] Holland Computing Center, University of Nebraska-Lincoln, Lincoln, NE 68588, USA
[3] Department of Mechanical Engineering, The University of Hong Kong, Hong Kong, People's Republic of China
[4] Department of Chemistry, University of Nebraska-Lincoln, Lincoln, NE 68588, USA
[5] Oak Ridge National Laboratory, Oak Ridge, TN 37831, USA
[6] State Laboratory of Hydraulic Machinery Transients, Ministry of Education, Wuhan, Hubei, 430072, People's Republic of China

E-mail: zhang@unl.edu and yyue@whu.edu.cn

Received 27 September 2016, revised 31 October 2016
Accepted for publication 7 November 2016
Published 14 December 2016

Abstract

In this work, thermal transport at the junction of an asymmetric layer hexagonal boron-nitride (*h*-BN) heterostructure is explored using a non-equilibrium molecular dynamics method. A thermal contact resistance of 3.6×10^{-11} K · m^2 W^{-1} is characterized at a temperature of 300 K with heat flux from the trilayer to monolayer regions. The mismatch in the flexural phonon modes revealed by power spectra analysis provides the driving force for the calculated thermal resistance. A high thermal rectification efficiency of 360% is calculated at the layer junction surpassing that of graphene. Several modulators, i.e. the system temperature, contact pressure and lateral dimensions, are applied to manipulate the thermal conductance and rectification across the interfaces. The predicted thermal rectification sustains positive correlations with temperature and phonon propagation lengths with little change to the coupling strength.

Keywords: hexagonal boron nitride, interfacial thermal resistance, thermal rectification, molecular dynamics, phonon thermal transport

(Some figures may appear in colour only in the online journal)

1. Introduction

The novel properties of low-dimensional materials have attracted enormous attention in recent years, and offer promising opportunities for low-energy and high-efficiency nanodevices. Among those materials, graphene stands out with its extraordinary thermal and mechanical attributes [1–6]. Monolayer hexagonal boron-nitride (*h*-BN), which is also known as 'white graphite', is a 2D analog of graphene and has a similar hexagonal honeycomb lattice structure. Its superb properties include low thermal expansion, a low dielectric constant and an ability to bear high loads [7–10]. The thermal properties of monolayer *h*-BN have been characterized and predicted by both experimental and numerical studies. Using the noncontact micro-Raman spectroscopy method, Zhou *et al* [11] measured the thermal conductivity (κ) of few-layer *h*-BN sheets in the range from 227–280 W m · K^{-1}. The thermal conductivity of suspended few layer *h*-BN was measured using a microbridge device with built-in resistance thermometers as well [12]. The reported κ values were from 250–360 W m · K^{-1} at room temperature. A much lower in-plane thermal conductivity of 20 W m · K^{-1} was

[7] Author to whom any correspondence should be addressed

reported for *h*-BN laminates using a laser flash method [13]. In addition, the κ of *h*-BN nanoribbons is predicted as 260–380 W m · K^{-1} with equilibrium molecular dynamics (EMD) simulation [14]. A much lower thermal conductivity of 8.5 W m · K^{-1} was calculated by Platek *et al* [15] using the non-equilibrium molecular dynamics (NEMD) method. Another EMD work was conducted by Mortazavi *et al* [16] to investigate the thermal conductivity of polycrystalline *h*-BN. The calculated results ranged from 80–300 W m · K^{-1} at different temperatures. The thermal conductivities of infinitely long armchair and zigzag *h*-BN nanoribbons with reverse non-equilibrium molecular dynamics simulations were predicted to be 277.78 W m · K^{-1} and 588.24 W m · K^{-1} respectively [17].

The existing experimental/numerical studies only investigate the in-plane properties of *h*-BN, and most work only considering monolayer *h*-BN, even though *h*-BN is usually multilayered in reality [18, 19]. This is significant because multi-layered *h*-BN has thermal and mechanical properties that differ by orders of magnitude along the in-plane and out-of-plane directions. Owing to its excellent thermal and chemical stability, monolayer *h*-BN has great potential to be applied in devices operating under extreme conditions. However, just like graphene, the growth of single-layer *h*-BN structures with high purity still faces tremendous challenges, and asymmetric layer configurations in the out-of-plane direction are inevitable [20, 21]. Similar to those of graphene, mono and multilayer *h*-BN structures could have distinct thermal properties due to the suppression of out-of-plane flexural phonons. An extremely low thermal conductivity of 0.3 W m · K^{-1}, which is two orders of magnitude lower than that of suspended *h*-BN, is calculated by MD simulation when *h*-BN is surrounded by a silica environment [22]. Such a significant impact could bring about unexpected interfacial phenomena such as thermal rectification (TR) and thermal contact resistance (*R*). A TR efficiency of 40% was calculated between suspended and inhomogeneous encased graphene structures [23]. It was found that perturbations induced by substrate coupling significantly suppress the long wavelength flexural phonon mode in the encased graphene when compared with that in the suspended graphene. As a result, the in-plane phonons can transmit through the interfaces well, whereas low-frequency flexural phonon modes are reflected, leading to a nontrivial interfacial thermal resistance. Similarly, Zhong *et al* [24] calculated the TR ratio in asymmetric thickness graphene. The suppression of the flexural phonons in thicker regions reduces the phonon transmission rate from single layer graphene, which causes direction-dependent thermal transport. The objective of this study is to investigate the effects of asymmetric interfaces on the in-plane thermal transport of *h*-BN. Based on the above discussions, the suppression of flexural phonons in multilayer *h*-BN structures could bring about unexpected thermal properties such as interfacial thermal resistance and tunable thermal rectification in asymmetric layer heterojunctions.

Given the strong effects of out-of-plane structures on the thermal properties of *h*-BN, thermal transport across multilayer and monolayer *h*-BN heterostructures needs to be further explored. In this work, classical MD simulation is used to comprehensively investigate interfacial thermal transport across trilayer/monolayer *h*-BN junctions. Thermal contact resistance is calculated by NEMD simulations. Detailed dispersion relations and phonon density of states analyses are performed to help understand the predicted results. Thermal energy propagations in decomposed lateral (*x*, *y*) and out-of-plane (*z*) directions are revealed by spatio-temporal temperature evolutions. Modulations of the system temperature, contact pressure and dimension on the thermal rectification and interfacial thermal resistance are investigated.

2. Physical basis and modeling details

All simulations are performed using the large-scale atomic/molecular massively parallel simulator (LAMMPS) [25]. The empirical interatomic potentials (EIP) need to be carefully selected in order to reproduce accurate thermal properties. The thermal conductivity depends sensitively on the accuracy of the acoustic phonon frequencies near the Brillouin zone center where the longitudinal- (LA) and transverse-acoustic (TA) velocities and the quadratic curvature of the out-of-plane acoustic (ZA) branch are determined. The Tersoff EIP used in this work has been specifically tuned and optimized to describe monolayer hexagonal boron-nitride structures. Parameters were carefully selected by minimizing the differences between the density functional theory calculation results and the force-field-derived total energy change per interface area for each displacement for each structure simultaneously, by updating the force field parameters using a genetic algorithm [14, 26]. It has therefore been widely applied to the investigation of the mechanical [27–30] and thermal [31–35] properties of *h*-BN and boron-nitride nanotubes. On the other hand, the Lennard–Jones (LJ) potential has also been widely used to describe the van der Waals (vdW) interactions in micro/nanoscale heterostructures. For semiconductor-type 2D materials such as hexagonal boron-nitride, the main energy carrier in the system is phonon, i.e. lattice vibrations. The lattice vibrations caused by vdW interactions can be accurately modeled with LJ EIP since the atom motions are solely determined by the forces exerted. For hybrid systems with electrons involved, the LJ EIP is insufficient to describe the system since the couplings between the electron–phonon require stochastic force. Since only phonon–phonon interactions exist in the current *h*-BN system, the LJ potential is selected to model the interactions between the *h*-BN layers. The interfacial thermal conductance between carbon nanotubes (CNTs) and graphene vdW junctions is calculated by Shi *et al* [36] using the LJ potential. It is reported that the phonon density of states of CNTs and graphene can be accurately predicted. Liu *et al* [37, 38] calculated the thermal resistance between graphene/silicene and graphene/MoS_2 vdW structures using the LJ potential. Other applications include graphene/3C-SiC [39], graphene/4H-SiC [40], graphene/*h*-BN [10], silicene/SiO_2 [41], graphene/silicon [5] and phosphorene/silicon [42]. The couplings

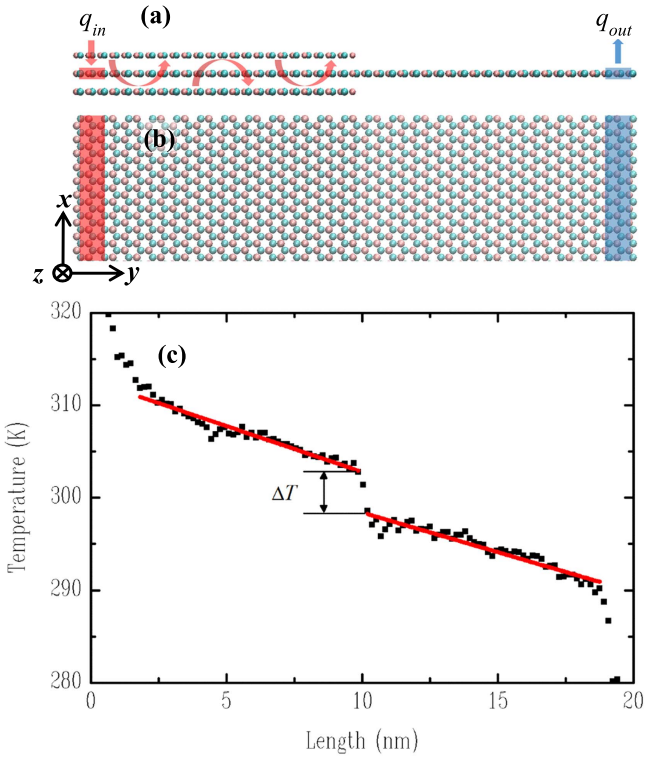

Figure 1. (a)–(b) A side view and top view of the asymmetric layer *h*-BN atomic structures. The outermost layer of the atoms at both ends is fixed. The red and blue shaded areas denote the heat source and heat sink respectively. (c) The temperature distribution of *h*-BN in the length direction at a steady state.

between different *h*-BN layers are modeled by the van der Waals potential which can be expressed as

$$V(r) = 4\chi\varepsilon\left[\left(\frac{\sigma}{r}\right)^{12} - \left(\frac{\sigma}{r}\right)^{6}\right], \quad (1)$$

where σ is the distance parameter, ε is the energy parameter and r is the interatomic distance. Parameter χ is used to adjust the coupling strength. The LJ parameters are calculated from the universal force field (UFF) [43], where $\varepsilon_{BB} = 7.816$ meV, $\sigma_{BB} = 3.638$ Å; $\varepsilon_{BN} = 4.839$ meV, $\sigma_{BN} = 3.444$ Å; $\varepsilon_{NN} = 2.996$ meV, $\sigma_{NN} = 3.261$ Å. The periodic boundary condition is applied in the width (x) direction to eliminate the size effect. Free boundary conditions are used in the length (y) direction and out-of-plane (z) direction. The time step is 0.5 fs for all calculations.

To calculate the interfacial thermal resistance at the asymmetric layer junction, an *h*-BN monolayer with dimensions of 4.9×19.9 ($x \times y$) nm^2 is first constructed. The monolayer is then evenly split into two halves in the length direction. The left portion is sandwiched between two *h*-BN nanoribbons, which forms a trilayer structure, and the right portion is freely suspended. The atomic configuration of the heterostructure is shown in figures 1(a) and (b). For thermal equilibrium calculations, the hybrid system was initially placed in a canonical ensemble (*NVT*) at a temperature of 300 K for 300 ps. A consecutive micro-canonical ensemble (*NVE*) was applied for another 200 ps for structural relaxation. A constant heat flux of 1.9×10^{-7} W was added/subtracted in the heating and cooling areas for another 4 ns to build a steady-state temperature gradient. The last 2 ns was used for data collection and temperature analysis. To obtain the R results in the opposite direction, the heating and cooling areas were reversed. The interfacial thermal resistance can be calculated using equation: $R = \Delta T \cdot A/q$, where A is the cross-sectional area and q is the imposed heat flux. The thickness of *h*-BN is chosen as 3.3 Å, which is also the interlayer spacing in bulk hexagonal BN crystals [44].

3. Results and discussions

3.1. Interfacial thermal resistance characterization

The temperature distributions along the heat flux direction in the mid-layer *h*-BN structure are shown in figure 1(c). A large temperature drop ΔT is observed across the junction area. To accurately obtain the temperature difference, linear fittings are applied to the temperature profiles on both sides and the end values are used to calculate ΔT. The predicted R at temperature 300 K with q in the positive y direction is 3.6×10^{-11} K · m^2 W^{-1}. The temperature profiles around the thermal reservoirs have non-linear trends and are excluded from the fitting processes. This non-linear phenomenon is caused by the ultra-fast kinetic energy exchange near these regions and the non-equilibrium between the kinetic and potential energies, and has also been observed in other materials such as graphene, carbon nanotubes, phosphorene, SiC and silicon using the NEMD method [45–48].

To illustrate thermal energy propagation in the hybrid structure, a 50 fs thermal impulse is imposed on the right end of the mid-layer *h*-BN after the system reaches thermal equilibrium. Local temperatures in the heating regions rise to ~1000 K while the rest of the system remains at 300 K. The spatiotemporal evolutions of the system temperature are recorded for the next 20 ps and depicted in figure 2(a). It has been proved that the in-plane and out-of-plane phonons in *h*-BN have different thermal transport capacities [49]. Therefore, the decomposed thermal contours in the x, y and z directions are calculated separately and shown in figures 2(b)–(d). It can be observed that the thermal energies in the in-plane transverse (TA) and longitudinal phonons (LA) can transmit across the asymmetric junction with nearly no reflections. However, the out-of-plane flexural mode (ZA) phonons have a significantly lower transmission rate compared with the TA and LA phonons. The thermal energies of the ZA phonons are confined to the upper portion of the thermal map, indicating a thermal barrier at the junction which is exhibited as the interfacial thermal resistance. Details will be further explained in the following discussions. Another important phenomenon shown in figure 2(d) is the much more condensed thermal energy conveyed by the ZA phonons compared to those in figures 2(b) and (c). This demonstrates the fact that in the *h*-BN structure, the out-of-plane flexural phonons make major contributions to its thermal conductivity. Similar results have also been reported for monolayer graphene [50–52].

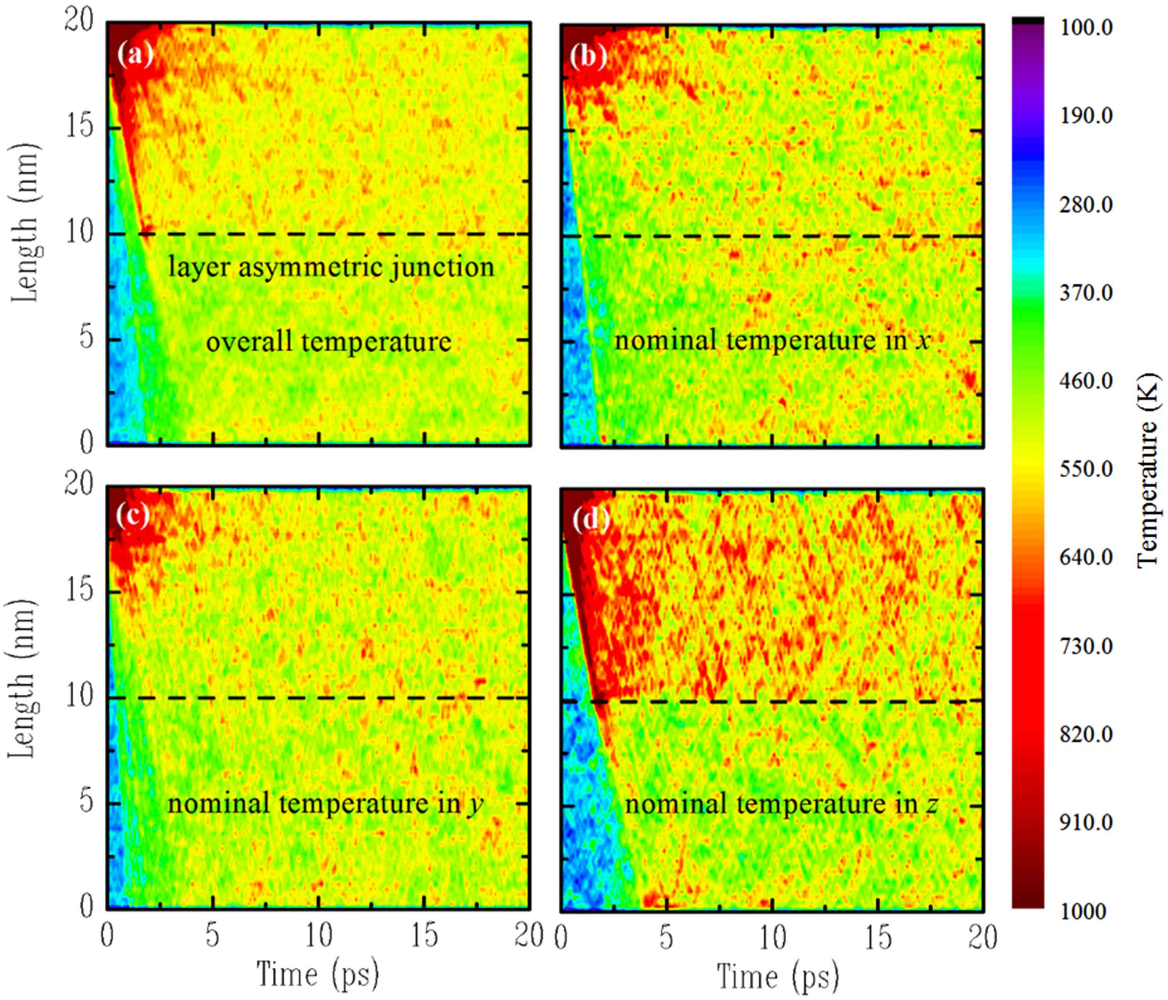

Figure 2. Spatiotemporal temperature evolution from the monolayer *h*-BN to the sandwiched *h*-BN after an ultrafast heat impulse. Figures (a)–(d) represent the temperatures in all directions—*x* direction, *y* direction and *z* direction—respectively.

3.2. Phonon spectrum analyses

The fundamental mechanism of interfacial thermal resistance at the asymmetric *h*-BN junction can be well understood from its dispersion relations in the *k*-space. The dispersion relations can be computed by taking a two dimensional Fourier transform of the time history of the velocity field [53], which can be expressed as

$$\phi(k, \omega) = \left| \frac{1}{N} \int v_\alpha \exp(\mathrm{i}ky - \mathrm{i}\omega t) \mathrm{d}t \mathrm{d}y \right| (a = x, y, z), \quad (2)$$

where N is the number of atoms in the system, y is the heat conduction direction, k is the wave vector, and ω is the phonon frequency. The velocity vector v_α is projected in the x, y and z directions to calculate the phonon energy density for the individual phonon modes respectively. The dispersion relations of the TA, LA and ZA phonons for monolayer *h*-BN are shown in figures 3(a)–(c). The corresponding counterparts for sandwiched *h*-BN are displayed in figures 3(d)–(f). Based on the calculated dispersion relations, the in-plane transverse and longitudinal phonons are found to have nearly the same formations for both the trilayer structure (left) and monolayer structure (right) of the *h*-BN, while for the flexural phonons, a significant shift at the k_0 point is found in the sandwiched *h*-BN regions. Similar results have also been observed in supported silicene [54] and graphene [23, 55] systems. In a similar way to graphene, the shift is caused by the broken reflection symmetry in *h*-BN, which significantly restricts the phase space for the phonon–phonon scattering of the flexural modes [56]. The variation is also partially attributed to the vdW interactions between the sandwiched *h*-BN layers, which affect the interatomic force constant of *h*-BN. The dispersion relation discrepancies in the ZA phonons soundly explain the thermal energy reflections in figure 2(d). Due to the phonon frequency mismatch in the out-of-plane direction, the phonon energies cannot fully transmit across the asymmetric layer junction, and this provides the driving force for the interfacial thermal resistance.

To further analyze the thermal properties in the heterostructure, the phonon density of states (PDOS) on both sides of the mid-layer *h*-BN are calculated. The PDOS $G(\omega)$ is calculated from the Fourier transform of the velocity autocorrelation function (VACF):

$$G(\omega) = \frac{1}{\sqrt{2\pi}} \int_{-\infty}^{\infty} \frac{\langle v(0) \cdot v(t) \rangle}{\langle v(0) \cdot v(0) \rangle} \mathrm{e}^{\mathrm{i}\omega t} \mathrm{d}t, \quad (3)$$

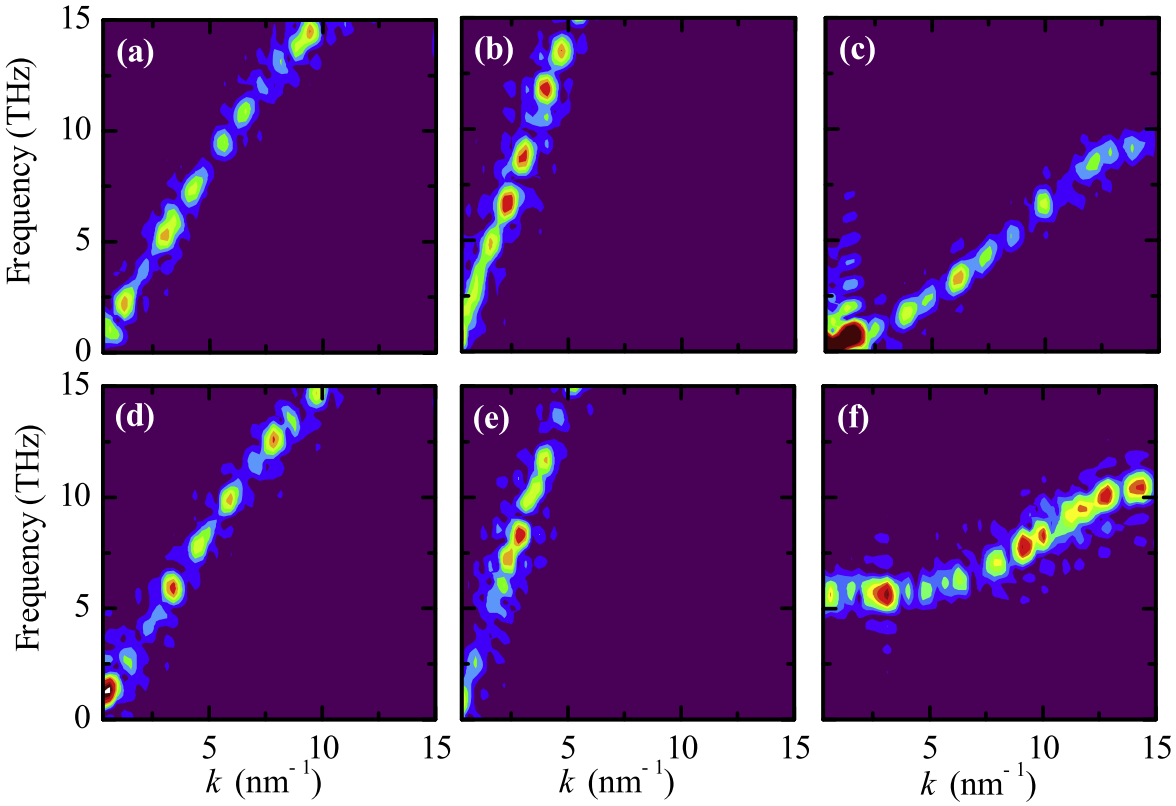

Figure 3. (a)–(c) The dispersion relations of the TA, LA and ZA phonons in monolayer *h*-BN. (d)–(f) The dispersion relations of TA, LA and ZA phonons in sandwiched *h*-BN.

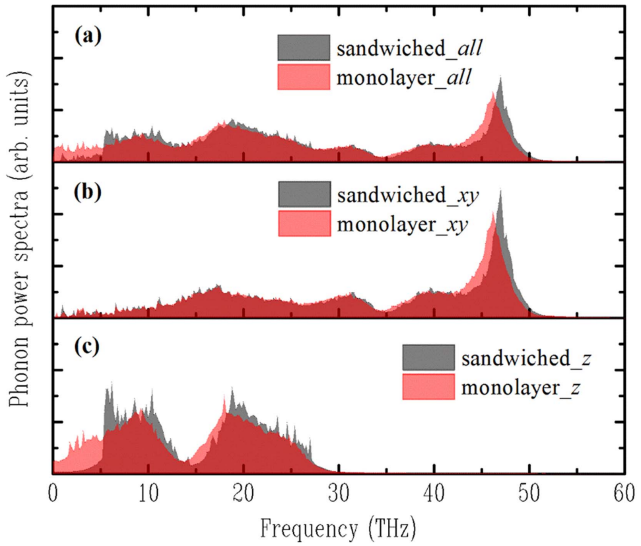

Figure 4. Phonon power spectra of the sandwiched and monolayer *h*-BN in different directions. (a) The overall PDOS; (b) lateral *xy* directions; (c) out-of-plane *z* direction.

where ω is the vibrational frequency, and $v(t)$ denotes the atom velocity at time t. Higher values of PDOS for a phonon with frequency ω mean more occupied states and zero PDOS means there is no phonon with a frequency ω existing in the system. Phonon power spectrum analysis provides a quantitative means to assessing the power carried by phonons in a system. Due to the differences in TA/LA and ZA phonons, the decomposed in-plane *xy* and out-of-plane *z* are calculated separately. The results are shown in figures 4(a)–(c). The major difference between the PDOS profiles of sandwiched and monolayer *h*-BN comes from the ZA phonons, as shown in figure 4(c). Phonon frequencies below 5 THz in the ZA branch are strongly suppressed in the sandwiched *h*-BN structure. The predicted phonon mismatch coincides with previous discussions about isothermal contours and dispersion relations. As shown in the following discussions, the PDOS can quantitatively describe thermal rectification and provides extra insights into the calculated interfacial thermal resistance.

3.3. Effects of temperature on thermal rectification

When q is applied in the negative y direction, the calculated R_{r2l} equals 8×10^{-11} K · m^2 W^{-1} at 300 K, as opposed to 3.6×10^{-11} K · m^2 W^{-1} (R_{l2r}) when q is in the positive y direction. Therefore, it can be concluded that the thermal energy flows preferably from the trilayer to monolayer areas. The thermal rectification efficiency (η), which is defined as $\eta = R_{r2l}/R_{l2r}$, equals 222% for *h*-BN at 300 K. Vallabhaneni *et al* [57] studied the thermal rectification at the carbon nanotube (CNT)/graphene nanoribbon (GNR) and silicon interfaces, the calculated η results varying from 106% ∼ 126% depending on the filling ratios of CNTs and GNRs. Using the NEMD method, Xu *et al* [23] calculated η between encased and free-standing graphene from 110%–150%. Wang *et al* [58] calculated the thermal rectification of different nanostructures such as nanofilm, nanowire and

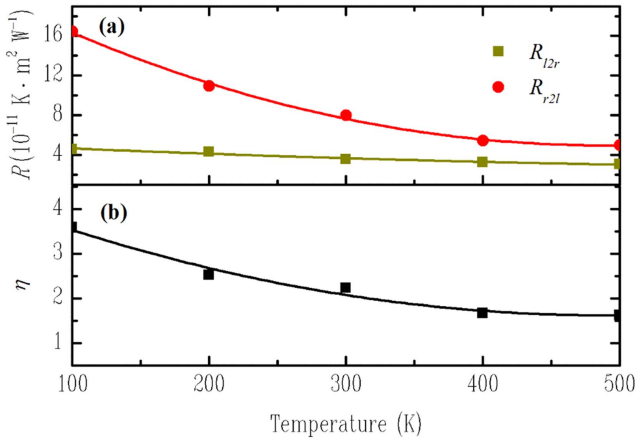

Figure 5. (a) The temperature dependence of thermal resistance in opposite heat flux directions. (b) Thermal rectification efficiency with the temperature from 100 K–500 K; the second order polynomial fitting is used as a visual aid.

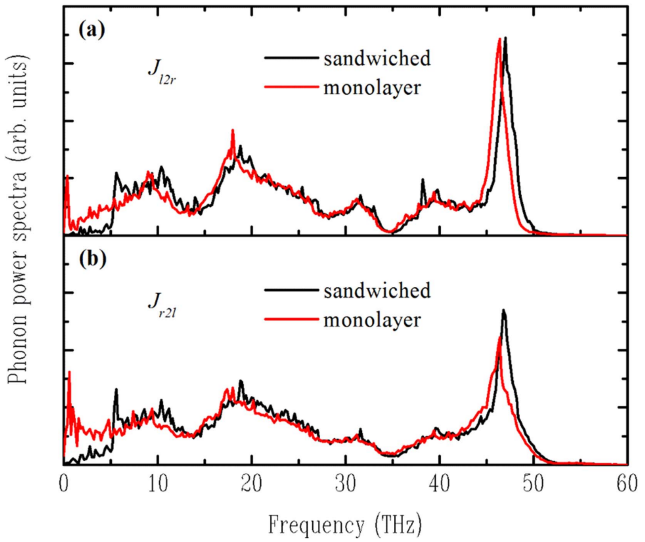

Figure 6. The phonon power spectra of sandwiched and monolayer *h*-BN after the heat flux *q* reaches a steady state in (a) the positive *y* direction and (b) the negative *y* direction.

asymmetric nanoribbons. The predicted η ranges from 110%–139%. The superb thermal rectification ratio of asymmetric layer *h*-BN exceeds those of the above-mentioned materials, indicating its great potential as an effective thermal rectifier in nanoelectronics.

In practical applications, a thermal rectifier could be placed under different working temperatures (T). Therefore, it is necessary to explore the dependence of R and η on T. Aside from the 300 K used in previous calculations, temperature values of 100, 200, 400 and 500 K are applied and the calculated results are shown in figure 5. Both R and η have a monotonic decreasing trend with an increasing system temperature. The calculated η reaches its maximum value of 360% at a temperature of 100 K. A decreasing trend of R with temperature has also been reported in other heterostructures such as graphene/*h*-BN [49], graphene/silicene [59], graphene/MoS_2 [38] and silicene/Si [41]. As the temperature of the system increases, the overall phonon population increases in the hybrid system and more phonons are involved in the thermal transport processes. The phonon mean free path becomes shorter at higher temperatures due to the higher number of phonons and an increased number of in-plane anharmonic phonon–phonon scattering events. The Umklapp scattering in lateral directions increases with temperature and boosts the phonon population at low frequencies, which directly enhances thermal transport across the junction. Correspondingly, the thermal rectification ratio is reduced due to the less significant phonon property differences. The interfacial thermal resistance calculated by the conventional acoustic mismatch model (AMM) and diffuse mismatch model (DMM) is independent of temperature within the classical high temperature limit. This is because the only temperature-dependent parts for both models are the distribution functions, whereas inelastic scatterings are not considered at the interfaces. The NEMD approach applied in this work accounts for both elastic and inelastic scatterings at the interface. It has been proved that at vdW heterojunctions, inelastic scattering provides the major contribution to the energy transport, surpassing that of elastic scattering at high temperatures [60]. The overall phonon population increases with temperature, which directly facilitates the interfacial thermal conductance and reduces the predicted thermal resistance. The phonon population increment is attributed to two major factors: (1) more phonon modes are excited at higher temperatures; (2) due to the enhanced Umklapp phonon scattering, some high-frequency phonons are scattered into multiple low frequency phonon branches.

3.4. Effects of coupling strength and system dimension

Since the underlying mechanism of thermal rectification in a hetero lattice system comes from the mismatch of energy spectra along the thermal transport direction, the PDOS of both sandwiched and monolayer *h*-BN are calculated after the system reaches a steady state under a constant heat flux q. The integration area for all profiles is normalized to unity for comparison. Figures 6(a) and (b) show the PDOS results with q imposed in positive and negative y directions respectively. The overlap can be calculated by

$$S = \frac{\int_0^\infty p_{\mathrm{A}}(\omega)p_{\mathrm{B}}(\omega)\mathrm{d}\omega}{\int_0^\infty p_{\mathrm{A}}(\omega)\mathrm{d}\omega\int_0^\infty p_{\mathrm{B}}(\omega)\mathrm{d}\omega}, \tag{4}$$

where $p_{\mathrm{A}}(\omega)$ and $p_{\mathrm{B}}(\omega)$ represent the phonon power spectra of sandwiched and monolayer *h*-BN, and S is the arbitrary unit overlap factor. The predicted S_{l2r} and S_{r2l} are 0.028 and 0.023 respectively. The larger PDOS overlap value in the positive y direction suggests better phonon couplings at the junction, which results in smaller thermal resistance.

The interlayer interaction effect in multilayer systems also plays a vital role during interfacial thermal transport. The composite materials are normally squeezed into compact spaces for optimal structural configurations. The effect of contact pressure on thermal performance at the asymmetric

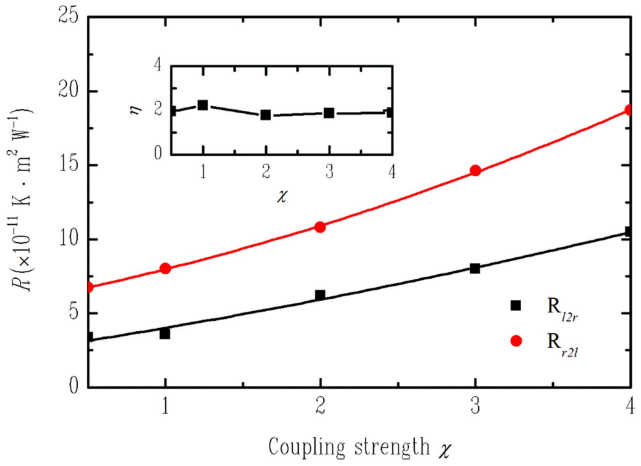

Figure 7. The dependence of R with coupling strength. The predicted interfacial thermal resistance increases monotonically with χ in both directions. The inset shows the thermal rectification variation with χ.

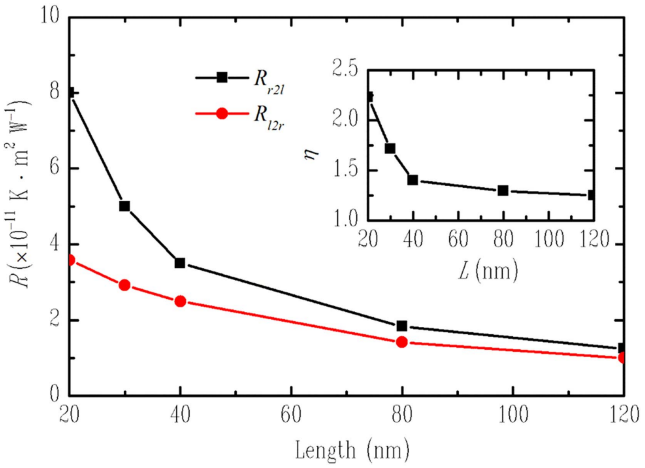

Figure 9. The effects of length on interfacial thermal resistance and thermal rectification. The insets shows the thermal rectification variation with length.

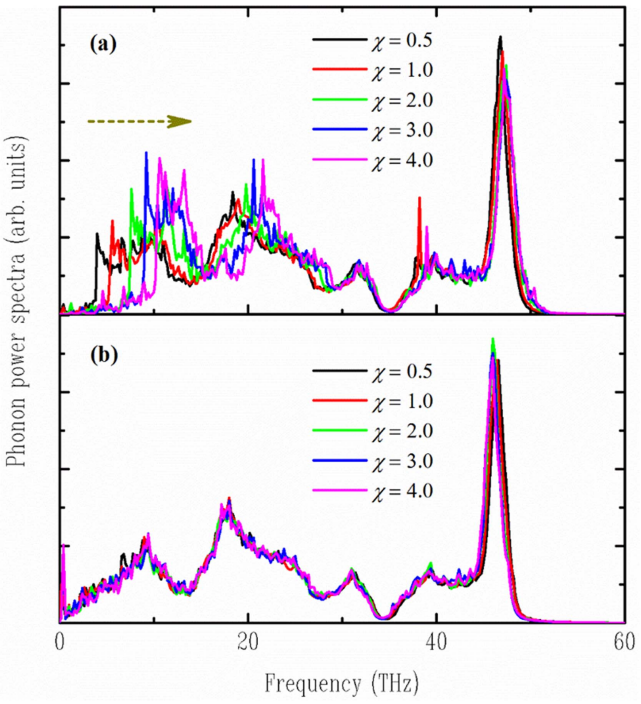

Figure 8. The phonon power spectra of (a) the sandwiched h-BN and (b) the monolayer h-BN with different coupling strengths.

layer junction is investigated by adjusting the coupling strength χ in the 12-6 LJ potential. Various χ values from 0.5 to 4 are used and the predicted results are shown in figure 7. It is observed that the interfacial thermal resistances in both directions increase monotonically with coupling strength. For q in the positive y direction, R_{l2r} increases from $3.4 \times 10^{-11}\,\mathrm{K\cdot m^2\,W^{-1}}$ to $1.0 \times 10^{-10}\,\mathrm{K\cdot m^2\,W^{-1}}$, while for q in the opposite direction, R_{r2l} changes from $6.7 \times 10^{-11}\,\mathrm{K\cdot m^2\,W^{-1}}$ to $1.9 \times 10^{-10}\,\mathrm{K\cdot m^2\,W^{-1}}$. The thermal rectification efficiency, as shown in the inset of figure 7, has fewer variations ranging from 180%–220% compared to the effect of the temperature. To help explain the calculated results, the PDOS of the sandwiched and monolayer h-BN are calculated for all cases. Figure 8(a) shows that as the coupling strength increases, the suppression of lower frequency phonons in sandwiched h-BN becomes much stronger. An obvious blue shift for the phonon power spectra is denoted in figure 8(a). For the monolayer regions, the calculated PDOS has no obvious changes. The increase of coupling strength causes a stronger phonon mismatch between the sandwiched and monolayer h-BN layers, which results in higher interfacial thermal resistance. Based on the above discussions, it is concluded that thermal rectification at the asymmetric layer h-BN junction decreases significantly with temperature, but is insensitive to coupling strength. On the other hand, the calculated R value decreases with temperature, but increases with coupling strength.

When the heat transfer lengths are smaller than the material's intrinsic phonon mean free path, the predicted thermal properties are dependent on the dimensions of the system due to the confined spaces. Therefore, it is also necessary to explore the effect of size on interfacial thermal resistance. Figure 9 shows the dependence of R on the hybrid system length (L). Different L values from 20 to 120 nm are used. It is found that R decreases monotonically with an increasing L. The thermal rectification ratio also decreases with system length, as shown in figure 9 inset. Such results have also been reported in previous numerical studies on silicene/graphene [59], graphene/graphene [23], CNT/Si [61] and SiO_2/Si [62]. As the system length increases, phonons with a larger wavelength will be excited and start to contribute to the interfacial thermal transport. Compared to the phonons with a shorter wavelength, these phonons can transmit across the thermal junction with less boundary scattering, resulting in smaller thermal resistance.

4. Conclusion

Using the NEMD method, the thermal resistance and rectification of asymmetric layer h-BN heterostructures are

investigated systematically. The thermal energy preferably flows from the trilayer to the monolayer regions, which gives a thermal resistance of $3.6 \times 10^{-11}\,\mathrm{K}\cdot\mathrm{m}^2\,\mathrm{W}^{-1}$ at 300 K compared to $8 \times 10^{-11}\,\mathrm{K}\cdot\mathrm{m}^2\,\mathrm{W}^{-1}$ in the opposite direction. Different modulators, such as the system temperature, contact pressure and lateral dimensions, are applied to effectively manipulate the thermal conductance at the interface. The calculated thermal resistance decreases with temperature and system length, but increases with out-of-plane vdW coupling strengths. On the other hand, thermal rectification efficiency can be enhanced by lowering the system temperature or reducing the system size, but is insensitive to coupling strengths. Detailed dispersion relation and phonon density of states analyses confirm that the mismatch in the flexural phonon mode is the main reason for the calculated thermal resistance, while the in-plane LA/TA phonons make negligible contributions. The spatiotemporal temperature evolutions in *h*-BN illustrate that the flexural phonons are the main energy carriers and convey the most thermal energy during interfacial thermal transport. Our results provide reasonable guidelines for the development and application of *h*-BN-based nanodevices.

Acknowledgments

This work was partially conducted in the Micro/Nanoscale Thermal Characterization Lab at the School of Power and Mechanical Engineering, Wuhan University, China, and the Holland Computing Center at the University of Nebraska-Lincoln, USA. Support from the Holland Computing Center University of Nebraska-Lincoln and the National Natural Science Foundation of China (nos. 51428603, 51576145 and 51279145) is greatly appreciated.

References

[1] Xin G Q, Yao T K, Sun H T, Scott S M, Shao D L, Wang G K and Lian J 2015 Highly thermally conductive and mechanically strong graphene fibers *Science* **349** 1083–7

[2] Zhang J, Huang X, Yue Y, Wang J and Wang X 2011 Dynamic response of graphene to thermal impulse *Phys. Rev.* B **84** 235416

[3] Zhang J, Xu F, Hong Y, Xiong Q and Pan J 2015 A comprehensive review on the molecular dynamics simulation of the novel thermal properties of graphene *RSC Adv.* **5** 89415–26

[4] Zhang J and Wang X 2013 Thermal transport in bent graphene nanoribbons *Nanoscale* **5** 734–43

[5] Zhang J, Wang Y and Wang X 2013 Rough contact is not always bad for interfacial energy coupling *Nanoscale* **5** 11598–603

[6] Lin H, Xu S, Zhang Y-Q and Wang X 2014 Electron transport and bulk-like behavior of Wiedemann–Franz law for sub-7 nm-thin iridium films on silkworm silk *ACS Appl. Mater. Interfaces* **6** 11341–7

[7] Weng Q H, Wang X B, Zhi C Y, Bando Y and Golberg D 2013 Boron nitride porous microbe its for hydrogen storage *ACS Nano* **7** 1558–65

[8] Sevik C 2014 Assessment on lattice thermal properties of two-dimensional honeycomb structures: graphene, h-BN, h-MoS_2, and h-$MoSe_2$ *Phys. Rev.* B **89** 035422

[9] Hu S *et al* 2014 Proton transport through one-atom-thick crystals *Nature* **516** 227

[10] Zhang J, Hong Y and Yue Y 2015 Thermal transport across graphene and single layer hexagonal boron nitride *J. Appl. Phys.* **117** 134307

[11] Zhou H *et al* 2014 High thermal conductivity of suspended few-layer hexagonal boron nitride sheets *Nano Res.* **7** 1232–40

[12] Jo I, Pettes M T, Kim J, Watanabe K, Taniguchi T, Yao Z and Shi L 2013 Thermal conductivity and phonon transport in suspended few-layer hexagonal boron nitride *Nano Lett.* **13** 550–4

[13] Jin-Cheng Z *et al* 2016 High thermal conductivity of hexagonal boron nitride laminates *2D Mater.* **3** 011004

[14] Sevik C, Kinaci A, Haskins J B and Çağın T 2011 Characterization of thermal transport in low-dimensional boron nitride nanostructures *Phys. Rev.* B **84** 085409

[15] Platek B, Falat T and Felba J 2013 Study on thermal conductivity of boron nitride in hexagonal structure in atomistic scale by using non-equilibrium molecular dynamics technique *2013 14th Int. Conf. on Thermal, Mechanical and Multi-Physics Simulation and Experiments in Microelectronics and Microsystems (Eurosime)*

[16] Mortazavi B, Pereira L F C, Jiang J-W and Rabczuk T 2015 Modelling heat conduction in polycrystalline hexagonal boron-nitride films *Sci. Rep.* **5** 13228

[17] Tabarraei A 2015 Thermal conductivity of monolayer hexagonal boron nitride nanoribbons *Comput. Mater. Sci.* **108** 66–71

[18] Duclaux L, Nysten B, Issi J P and Moore A W 1992 Structure and low-temperature thermal conductivity of pyrolytic boron nitride *Phys. Rev.* B **46** 3362–7

[19] Shi Y *et al* 2010 Synthesis of few-layer hexagonal boron nitride thin film by chemical vapor deposition *Nano Lett.* **10** 4134–9

[20] Geim A K and Grigorieva I V 2013 Van der Waals heterostructures *Nature* **499** 419–25

[21] Levendorf M P, Kim C J, Brown L, Huang P Y, Havener R W, Muller D A and Park J 2012 Graphene and boron nitride lateral heterostructures for atomically thin circuitry *Nature* **488** 627–32

[22] Ni Y, Jiang J, Meletis E and Dumitrică T 2015 Thermal transport across few-layer boron nitride encased by silica *Appl. Phys. Lett.* **107** 031603

[23] Xu W, Zhang G and Li B 2014 Interfacial thermal resistance and thermal rectification between suspended and encased single layer graphene *J. Appl. Phys.* **116** 134303

[24] Zhong W-R, Huang W-H, Deng X-R and Ai B-Q 2011 Thermal rectification in thickness-asymmetric graphene nanoribbons *Appl. Phys. Lett.* **99** 193104

[25] Plimpton S 1995 Fast parallel algorithms for short-range molecular dynamics *J. Comput. Phys.* **117** 1–19

[26] Kınacı A, Haskins J B, Sevik C and Çağın T 2012 Thermal conductivity of BN-C nanostructures *Phys. Rev.* B **86** 115410

[27] Shijun Z and Jianming X 2013 Mechanical properties of hybrid graphene and hexagonal boron nitride sheets as revealed by molecular dynamic simulations *J. Phys. D: Appl. Phys.* **46** 135303

[28] Tongwei H, Ying L and Chengyuan W 2014 Effects of temperature and strain rate on the mechanical properties of hexagonal boron nitride nanosheets *J. Phys. D: Appl. Phys.* **47** 025303

[29] McGuigan B C, Pochet P and Johnson H T 2016 Critical thickness for interface misfit dislocation formation in two-dimensional materials *Phys. Rev.* B **93** 214103

[30] Le M-Q 2014 Young's modulus prediction of hexagonal nanosheets and nanotubes based on dimensional analysis and atomistic simulations *Meccanica* **49** 1709–19
[31] Jun S and Nikhil V M 2013 Thermal transport in lattice-constrained 2D hybrid graphene heterostructures *J. Phys. Condens. Matter* **25** 445007
[32] Tan S-H, Tang L-M and Chen K-Q 2014 Phonon scattering and thermal conductance properties in two coupled graphene nanoribbons modulated with bridge atoms *Physics Letters* A **378** 1952–5
[33] Ong Z-Y and Zhang G 2015 Efficient approach for modeling phonon transmission probability in nanoscale interfacial thermal transport *Phys. Rev.* B **91** 174302
[34] Ong Z-Y, Zhang G and Zhang Y-W 2016 Controlling the thermal conductance of graphene/*h*-BN lateral interface with strain and structure engineering *Phys. Rev.* B **93** 075406
[35] Loeblein M, Tay R Y, Tsang S H, Ng W B and Teo E H T 2014 Configurable three-dimensional boron nitride–carbon architecture and its tunable electronic behavior with stable thermal performances *Small* **10** 2992–9
[36] Shi J, Dong Y, Fisher T and Ruan X 2015 Thermal transport across carbon nanotube-graphene covalent and van der Waals junctions *J. Appl. Phys.* **118** 044302
[37] Liu B, Baimova J A, Reddy C D, Law A W-K, Dmitriev S V, Wu H and Zhou K 2014 Interfacial thermal conductance of a silicene/graphene bilayer heterostructure and the effect of hydrogenation *ACS Appl. Mater. Interfaces* **6** 18180–8
[38] Liu B, Meng F, Reddy C D, Baimova J A, Srikanth N, Dmitriev S V and Zhou K 2015 Thermal transport in a graphene-MoS_2 bilayer heterostructure: a molecular dynamics study *RSC Advances* **5** 29193–200
[39] Wang Z, Bi K, Guan H and Wang J 2014 Thermal transport between graphene sheets and SiC substrate by molecular-dynamical calculation *J. Mater.* **2014** 5
[40] Li M, Zhang J, Hu X and Yue Y 2015 Thermal transport across graphene/SiC interface: effects of atomic bond and crystallinity of substrate *Appl. Phys.* A **119** 415–24
[41] Zhang J, Hong Y, Tong Z, Xiao Z, Bao H and Yue Y 2015 Molecular dynamics study of interfacial thermal transport between silicene and substrates *Phys. Chem. Chem. Phys.* **17** 23704–10
[42] Zhang J, Hong Y, Liu M, Yue Y, Xiong Q and Lorenzini G 2017 Molecular dynamics simulation of the interfacial thermal resistance between phosphorene and silicon substrate *Int. J. Heat Mass Transfer* **104** 871–7
[43] Rappe A K, Casewit C J, Colwell K S, Goddard W A and Skiff W M 1992 UFF, a full periodic table force field for molecular mechanics and molecular dynamics simulations *J. Am. Chem. Soc.* **114** 10024–35
[44] Warner J H, Rümmeli M H, Bachmatiuk A and Büchner B 2010 Atomic resolution imaging and topography of boron nitride sheets produced by chemical exfoliation *ACS Nano* **4** 1299–304
[45] Wang S-C, Liang X-G, Xu X-H and Ohara T 2009 Thermal conductivity of silicon nanowire by nonequilibrium molecular dynamics simulations *J. Appl. Phys.* **105** 014316
[46] Zhang J, Wang X and Xie H 2013 Phonon energy inversion in graphene during transient thermal transport *Phys. Lett.* A **377** 721–6
[47] Zhang J, Wang X and Xie H 2013 Co-existing heat currents in opposite directions in graphene nanoribbons *Phys. Lett.* A **377** 2970–8
[48] Chen W, Zhang J and Yue Y 2016 Molecular dynamics study on thermal transport at carbon nanotube interface junctions: effects of mechanical force and chemical functionalization *Int. J. Heat Mass Transfer* **103** 1058–64
[49] Hong Y, Zhang J, Huang X and Zeng X C 2015 Thermal conductivity of a two-dimensional phosphorene sheet: a comparative study with graphene *Nanoscale* **7** 18716–24
[50] Hong Y, Zhang J and Zeng X C 2016 Thermal contact resistance across a linear heterojunction within hybrid graphene/hexagonal boron nitride sheet *Phys. Chem. Chem. Phys.* **18** 24164–170
[51] Seol J H *et al* 2010 Two-dimensional phonon transport in supported graphene *Science* **328** 213–6
[52] Prasher R 2010 Graphene spreads the heat *Science* **328** 185–6
[53] Shiomi J and Maruyama S 2006 Non-Fourier heat conduction in a single-walled carbon nanotube: classical molecular dynamics simulations *Phys. Rev.* B **73** 205420
[54] Wang Z Y, Feng T L and Ruan X L 2015 Thermal conductivity and spectral phonon properties of freestanding and supported silicene *J. Appl. Phys.* **117** 084317
[55] Qiu B and Ruan X 2012 Reduction of spectral phonon relaxation times from suspended to supported graphene *Appl. Phys. Lett.* **100** 193101
[56] Lindsay L, Broido D A and Mingo N 2010 Flexural phonons and thermal transport in graphene *Phys. Rev.* B **82** 115427
[57] Vallabhaneni A K, Qiu B, Hu J, Chen Y P, Roy A K and Ruan X 2013 Interfacial thermal conductance limit and thermal rectification across vertical carbon nanotube/graphene nanoribbon-silicon interfaces *J. Appl. Phys.* **113** 064311
[58] Wang Y, Vallabhaneni A, Hu J, Qiu B, Chen Y P and Ruan X 2014 Phonon lateral confinement enables thermal rectification in asymmetric single-material nanostructures *Nano Lett.* **14** 592–6
[59] Liu B, Baimova J A, Reddy C D, Dmitriev S V, Law W K, Feng X Q and Zhou K 2014 Interface thermal conductance and rectification in hybrid graphene/silicene monolayer *Carbon* **79** 236–44
[60] Stevens R J, Zhigilei L V and Norris P M 2007 Effects of temperature and disorder on thermal boundary conductance at solid–solid interfaces: nonequilibrium molecular dynamics simulations *Int. J. Heat Mass Transfer* **50** 3977–89
[61] Diao J, Srivastava D and Menon M 2008 Molecular dynamics simulations of carbon nanotube/silicon interfacial thermal conductance *J. Chem. Phys.* **128** 164708
[62] Chen J, Zhang G and Li B 2012 Thermal contact resistance across nanoscale silicon dioxide and silicon interface *J. Appl. Phys.* **112** 064319